Applied and
Computational
Mechanics

Adapting the control of the magnetic bearings of a highly flexible and gyroscopic rotor to the excitations by the motor

D. Franz[a,*], B. Schüßler[a], S. Rinderknecht[a]

[a]*Institute for Mechatronic Systems, TU Darmstadt, Otto-Berndt-Straße 2, 64287 Darmstadt, Germany*

Abstract

A test rig was built to perform fatigue tests on thick-walled cylinders made of fibre reinforced plastic (FRP). During the fatigue test, the rotational speed of an FRP cylinder is periodically varied until it fails. The FRP cylinder is connected to a drive spindle that accelerates and decelerates it using a permanent magnet synchronous machine (PMSM). To avoid excessive wear, the rotor is supported by active magnetic bearings (AMB). After the fatigue test was finished with the first cylinder, a new cylinder was attached to the test stand. With this new specimen, previously uncritical radial vibrations became more severe. For high accelerations, these vibrations led to instability of the rotor. However, high accelerations are desirable to perform the fatigue tests in the shortest possible time. Hence, the AMB control should be made insensitive to these vibrations. Since the vibrations depend on the acceleration of the rotor, it is reasonable to assume that they are induced by the PMSM. To reduce the vibrations, these excitations from the PMSM are included in the model-based controller parametrization process for the radial AMB, in which the parameters are adjusted via optimization. With the adjusted control, the amplitude of the vibration was significantly reduced and higher accelerations were possible. The described parameter tuning process can easily be adapted to different AMB systems with disturbances and changes in the system. © 2023 University of West Bohemia.

Keywords: active magnetic bearings, robust control, rotor dynamics, predefined controller structure

1. Introduction

Active magnetic bearings (AMB) use the force of an electric magnet to levitate the rotor [7, 22]. Since the rotor does not touch the stator and no friction occurs, the bearing shows low rotational losses and no wear. This makes AMB ideal for high rotational speeds and vacuum applications. AMB are open-loop unstable and need an active position control, which also provides the possibility to actively influence vibrations of the system.

For many AMB systems, a conventional decentralized proportional-integral-derivative (PID) controller is sufficient to stabilize it [17, 22, 30]. However, elastic or strongly gyroscopic rotors often require coupling of the controllers of multiple AMB and more sophisticated controller structures. The gyroscopic change of the rotor behavior with its rotational speed can be tackled by partially compensating the gyroscopic coupling [1, 14, 15, 33] or by adjusting the controller parameters with the rotational speed [5, 25]. However, these controllers require a reliable measurement of the rotational speed and are often difficult to implement for highly elastic rotors. For systems with multiple eigenmodes in the operation range, $\mathcal{H}_\infty$-control [13, 17, 20, 27, 31] and μ-synthesis [21, 24, 26, 29] are frequently used, which often result in high-order controllers.

The system discussed in this paper has four rotor eigenfrequencies in the operation range which strongly depend on its rotational speed (see Section 2). Furthermore, the measurement

---

*Corresponding author. Tel.: +49 615 116 231 52, e-mail: franz@ims.tu-darmstadt.de.

of its rotational speed might not always be reliable. The model-based controller design used for this system utilizes a predefined controller structure, whose parameters are tuned by means of optimization (cf. [8, 19]). The objective function of this optimization is the $\mathcal{H}_\infty$-norm of the generalized transfer function of the system (cf. [3]). This approach allows to consider uncertainties, limitations and the speed dependency of the system without gain scheduling and with a low controller order, i.e., low online computing time. A more detailed description of this approach will be shown in Section 3.2. It was developed and successfully applied to the system to reduce rotor heating [9]. However, during operation, rotor vibrations occurred which limited the performance of the system. The controller parametrization was adapted to counter these vibrations, which will be shown in Section 3.3. Experimental results will be shown in Section 4.

2. System

The test rig shown in Fig. 1 was designed and built to perform fatigue tests on thick-walled cylinders made of unidirectional fiber reinforced plastic (FRP), in which the fibers are oriented in tangential direction. These cylinders represent the rotors of outer-rotor flywheels (e.g., [6, 10, 23, 28, 32, 34]). During the fatigue test, the rotational speed of an FRP cylinder is periodically varied from 15 000 rpm to 30 000 rpm, until it fails or a maximum cycle count of 200 000 is reached. At 30 000 rpm, the radial compressive stress in the FRP reaches 120 MPa and the tangential tension 700 MPa. The FRP cylinder, which is the specimen, is connected to a drive spindle via an aluminium hub. An inverter-driven permanent magnet synchronous machine (PMSM) inside the spindle accelerates and decelerates the rotor. Parameters of the PMSM can be found in Table 1 in the Appendix. To avoid excessive wear, the rotor is supported by AMB. The radial AMB are designed as heteropolar bearings with a differential winding scheme. Therefore, there is one coil for the bias current and one coil for the control current in every pole pair. The control for the AMB is implemented on a field-programmable gate array. All analogue signals have an analogue first order low pass filter with a cut-off frequency of 5.6 kHz to reduce aliasing and are acquired with a sampling frequency of 40 kHz. The radial AMB are controlled
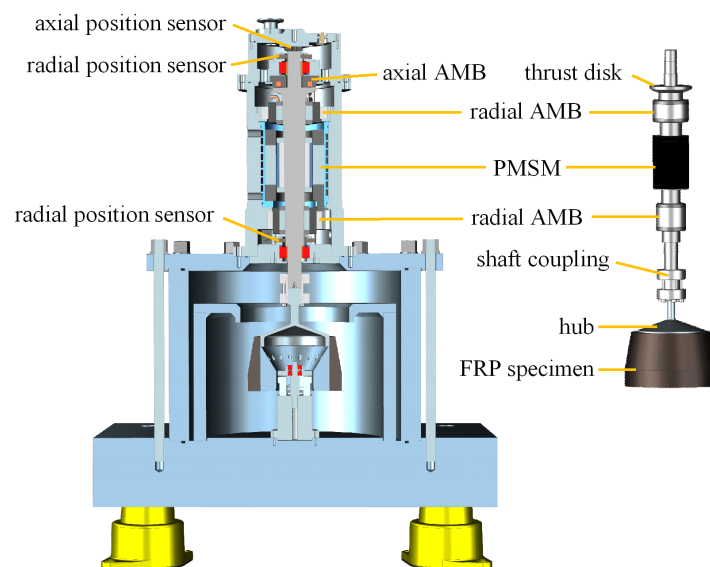
Fig. 1. Cross-section of the test rig (*left*), rotor with the specimen (*right*)

using the signals of eddy current positions sensors at the upper and lower end of the rotor (see Fig. 1) and currents sensors in the amplifier. More details on the test rig can be found in [9, 11].

The rotor with the FRP cylinder has four radial eigenfrequencies (EFs) below 1 kHz, which strongly depend on its rotational speed due to the gyroscopic behavior of the FRP cylinder. The corresponding first four eigenmodes (EMs) at 0 rpm are shown in Fig. 2a which were calculated using a volume finite element model of the rotor. A calculated Campbell-diagram is shown in Fig. 2b. Three of the forward EFs have to be passed to get to the operation range above 15 000 rpm. The fourth forward EF rises in such a way that it is not reached by the synchronous excitations in the operation range.

(a)   (b)
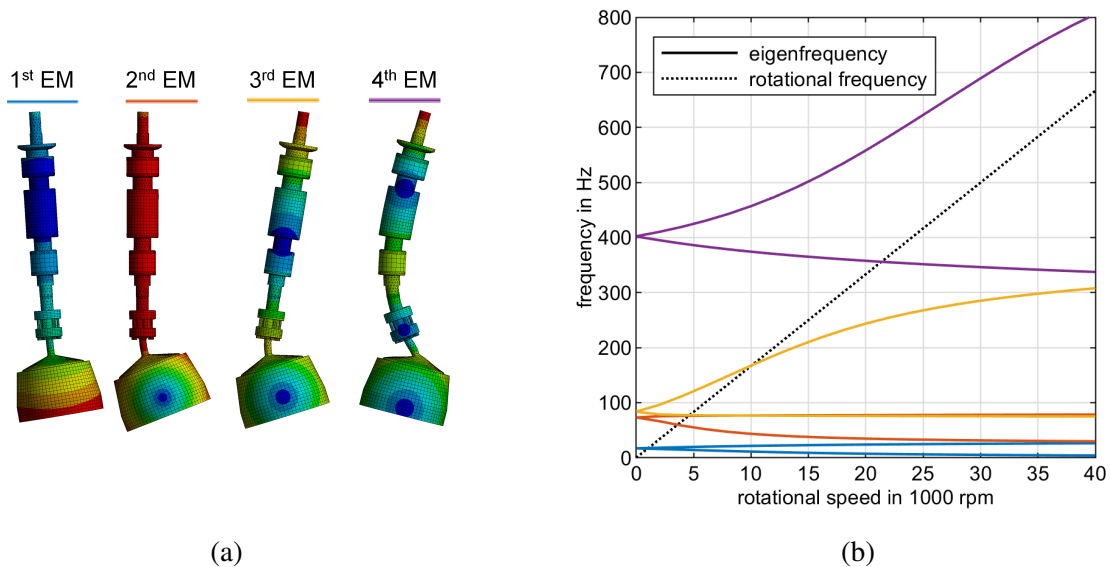
Fig. 2. (a) Radial eigenmodes (EMs) of the rotor at 0 rpm calculated using a 3D finite element model (FEM) (cf. [9]), (b) corresponding speed-dependent eigenfrequencies (EFs) calculated utilizing the FEM. The line colours correspond to those shown in (a) above the EMs

This speed-dependent behavior of the rotor as well as sensor noise and the limitations of the system have to be considered while designing the controller for the radial AMB. For the test rig, the parameters of a predefined controller structure were tuned using an optimization process, which is described in detail in [9]. The control of the axial AMB, which is decoupled from the radial direction, is less challenging and was tuned manually. A fatigue test with a first specimen was performed. The test was stopped after 134 270 cycles since the unbalance of the specimen was rapidly changing, which can be attributed to cracks in the FRP. Another fatigue test was started with a new specimen. However, with this new specimen previously un-critical acceleration-dependent radial vibrations became more severe. These can be seen in the Campbell-diagrams in Fig. 3 which were measured during run-ups with different acceleration rates. A labelled version of Fig. 3a can be found in Fig. 9 in the Appendix. The EFs of the rotor, as well as synchronous and higher harmonic vibrations, can be seen in all diagrams. However, further vibrations are visible as sidebands of the first harmonic, which are always 140 Hz above and, starting at 8 100 rpm, 135 Hz below the synchronous vibrations. The latter was particularly critical at around 23 000 rpm where it excited the third forward EF of the rotor. The amplitudes of these sidebands strongly depended on the acceleration rate. With 150 rpm/s, they were barely visible (see Fig. 3a), whereas they nearly destabilized the rotor with 1 000 rpm/s.
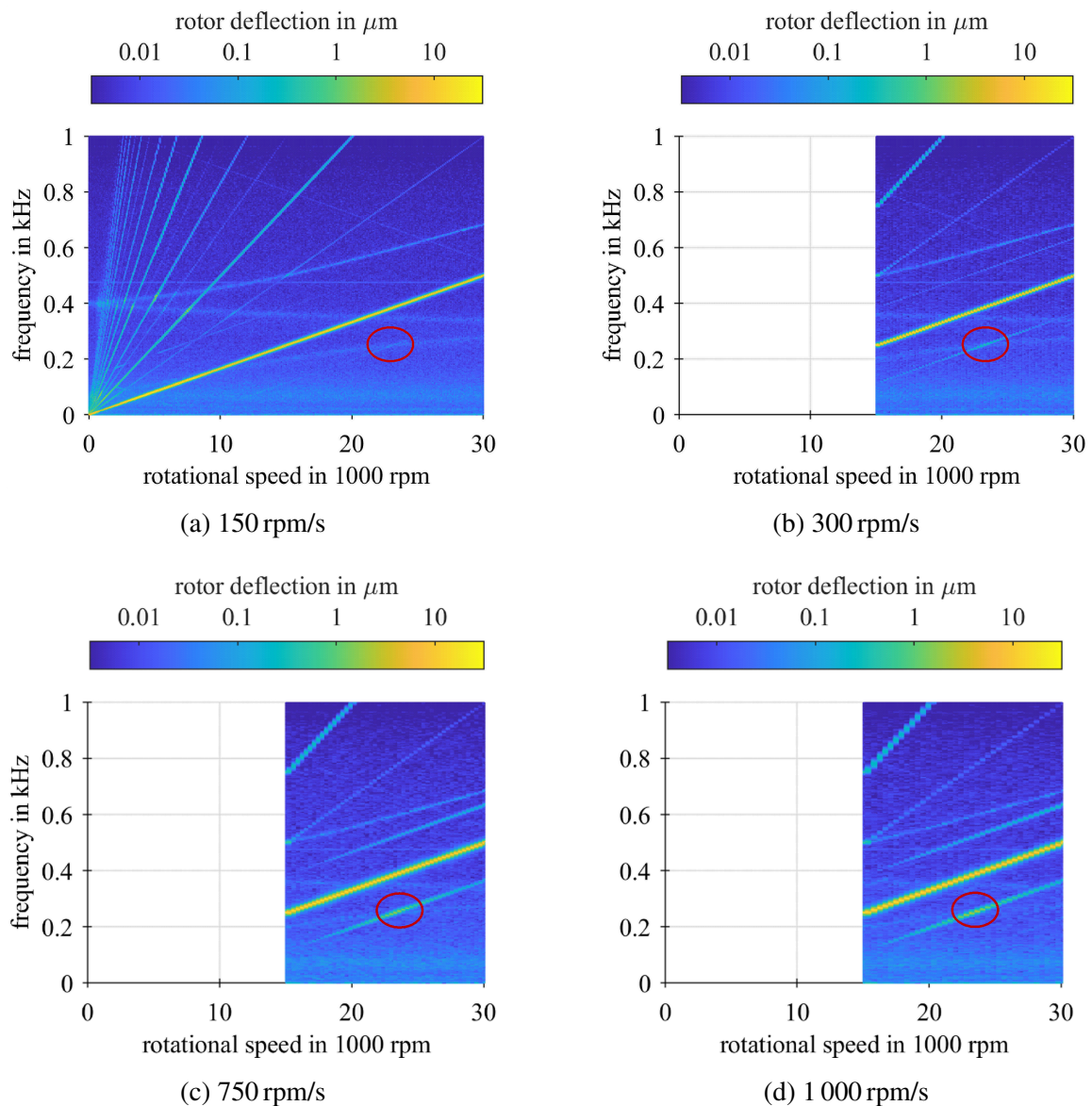
Fig. 3. Measured Campbell-diagram of the radial rotor displacement during a run-up (a) from 0 rpm to 30 000 rpm in 200 s, (b) from 15 000 rpm to 30 000 rpm in 50 s, (c) from 15 000 rpm to 30 000 rpm in 20 s, (d) from 15 000 rpm to 30 000 rpm in 15 s. The red circle marks the subharmonic excitation of the third eigenmode

The amplitude of the lower sideband and the 1st harmonic at the subharmonic resonance are summarized in Table 2 in the Appendix. As a result of the strong vibrations, only acceleration rates below 330 rpm/s could be used for the long-term test. Since the vibrations depended on the acceleration rate of the rotor and could be changed by the control of the PMSM, which however is not in the scope of this paper, it is reasonable to assume that they were induced by the PMSM. The fact that they caused problems with this specimen and not with the first may be due to deviations in the specimen geometry and associated shifts in the EMs or changes of the PMSM or its inverter.

To perform the fatigue tests in the shortest possible time, high acceleration rates are desirable. Hence, the AMB control had to be made insensitive to the sidebands. Since they only occur in radial direction and no influence of the axial AMB could be observed, this paper will

focus on the control of the radial AMB. In order to reduce the vibrations, the changed specimen geometry as well as the excitation by the PMSM were considered in the parametrization process of the radial AMB controller. An adaption of the parametrization process is shown in the next section and an experimental investigation of the results in Section 3. Since the sideband 135 Hz below the synchronous vibrations was more severe than the one above the synchronous vibrations, this paper will focus on the first.

3. Controller parametrization

A linear model of the plant is used for the controller parametrization, which is described in Section 3.1. The controller parametrization process is described in Section 3.2. The model and the parametrization process are described in more detail in [9]. The adaption of this process to the previously described vibrations is shown in Section 3.3.

3.1. Plant model

The plant model consists of various subsystems for the different components. These are elastic models for rotor and stator, a linearized model of the radial AMB and their amplifier (AMP), the negative radial stiffness of the PMSM as well as the position and current sensors, each with a low pass filter (LP) to reduce aliasing. All subsystems are represented by linear, rational transfer functions (TFs). The dynamic behavior of the gyroscopic rotor depends on its rotational speed Ω. Fig. 4 shows the interconnection between these subsystems in the overall plant model $\mathcal{P}(s, \Omega)$ with its inputs $\boldsymbol{F}_{un}$ and $\boldsymbol{U}_{set}$. The latter is the set voltage calculated by the controller. $\boldsymbol{F}_{un}$ contains rotational frequency harmonic disturbance forces on the rotor which are used to simulate the unbalance of the rotor. $\Delta\boldsymbol{q}$, $\boldsymbol{I}_c$, $\Delta\tilde{\boldsymbol{q}}_{sen}$ and $\tilde{\boldsymbol{I}}_c$ are the outputs of $\mathcal{P}(s, \Omega)$. $\Delta\boldsymbol{q}$ contains the relative rotor deflections, i.e., the difference between the radial deflections of the rotor $\boldsymbol{q}_r$ and the radial deflections of the stator $\boldsymbol{q}_s$. $\boldsymbol{I}_c$ is comprised of the control currents of the radial AMB. $\Delta\tilde{\boldsymbol{q}}_{sen}$ contains the measured and filtered relative rotor deflections and $\tilde{\boldsymbol{I}}_c$ the filtered control currents of the radial AMB. F_{AMB} is the radial force generated by the AMB and F_{PMSM} the radial force resulting from the negative stiffness of the PMSM. U is the output voltage of the AMP.

3.2. Controller parametrization framework

A time-invariant output feedback $\mathcal{C}(s)$ is used to stabilize the rotor in the AMB using the measured outputs $\Delta\tilde{\boldsymbol{q}}_{sen}$ and $\tilde{\boldsymbol{I}}_c$, which are combined in the vector $\boldsymbol{y}$. Hence, for an idealized system

Fig. 4. Structure of the plant model [9]

without noise, the controller output $\boldsymbol{u}$ is calculated by

$$\boldsymbol{u}(s) = -\mathcal{C}(s)\,\boldsymbol{y}(s) \tag{1}$$

and $\boldsymbol{u}$ is equal to $\boldsymbol{U}_{set}$. However, noise and disturbances should be considered in the controller parametrization process. To accomplish this, sensor noise $\boldsymbol{n}$ is added to $\boldsymbol{y}$ and a disturbance voltage $\boldsymbol{U}_d$ is added to $\boldsymbol{u}$ (see Fig. 5). $\boldsymbol{U}_d$ is used, among other things, to limit the influence of multiplicative model uncertainties [31, 35]. Hence, $\boldsymbol{U}_{set}$ is given by

$$\boldsymbol{U}_{set}(s) = \boldsymbol{u}(s) + \boldsymbol{U}_d(s) \tag{2}$$
$$\text{with } \boldsymbol{u}(s) = -\mathcal{C}(s)\,\tilde{\boldsymbol{y}}(s) \quad \text{and} \quad \tilde{\boldsymbol{y}}(s) = \boldsymbol{y}(s) + \boldsymbol{n}(s).$$

Furthermore, to incorporate frequency-dependent design goals and the limitations of the system in the parametrization process, stable weighting functions $\mathcal{W}$ are introduced for the disturbance inputs $\boldsymbol{F}_{un}$, $\boldsymbol{U}_d$ and $\boldsymbol{n}$ as well as the evaluation outputs $\Delta\boldsymbol{q}$, $\boldsymbol{I}_c$ and $\boldsymbol{u}$ (e.g., [18, 21, 22, 31]). The weighting functions are chosen in such a way that the maximum amplitudes of the inputs are one and the outputs have to be smaller or equal to one (see [9]). Finally, the disturbance inputs are combined in the vector $\boldsymbol{w}$ and the weighted evaluation outputs in the vector $\boldsymbol{z}$. This results in the weighted plant model $\mathcal{P}_{\mathcal{W}}(s, \Omega)$ as shown in Fig. 5.

Fig. 5. Weighted model of the plant with the controller [9]

Parameters of a predefined controller structure are adjusted during the parametrization process with the goal of minimizing the $\mathcal{H}_\infty$ norm of the TF-matrix $\mathcal{G}_{zw}$ from $\boldsymbol{z}$ to $\boldsymbol{w}$ of the controlled plant (cf. [3]), i.e.,

$$\min_{\mathcal{C}(s)} \|\mathcal{G}_{zw}(s)\|_\infty. \tag{3}$$

The optimization is performed using the function *hinfstruct* in MATLAB [4, 12]. To ensure that the closed loop is stable for all Ω in the speed range of the system, the controller parameters are tuned for multiple rotational speeds Ω_j at once [9, 12]. To accomplish this, several TFs of the plant at different Ω_j are connected in parallel. For example, for two rotational speeds Ω_1 and Ω_2, the goal of the optimization becomes

$$\min_{\mathcal{C}(s)} \left\|\mathrm{diag}\big(\mathcal{G}_{zw}(s, \Omega_1), \mathcal{G}_{zw}(s, \Omega_2)\big)\right\|_\infty, \tag{4}$$

which will minimize the maximum of the $\mathcal{H}_\infty$ norms of both systems [12]. The sensitivity function $\mathcal{S}$, which is given by

$$\mathcal{S}(s) = \frac{\Delta\tilde{\boldsymbol{q}}_{sen}(s) + \boldsymbol{n}(s)}{\boldsymbol{n}(s)}, \tag{5}$$

is also included in the optimization for different Ω_j with a corresponding weighting function $\mathcal{W}_\mathcal{S}$ to take into account the limits on its gain specified in [16]. Hence, the final optimization goal is

$$\min_{\mathfrak{c}(s)} \left\| \text{diag}\big(\mathcal{G}_{zw}(s, \Omega_1), \dots, \mathcal{G}_{zw}(s, \Omega_n), \mathcal{W}_\mathcal{S}(s)\,\mathcal{S}(s, \Omega_{n+1}), \dots, \mathcal{W}_\mathcal{S}(s)\,\mathcal{S}(s, \Omega_m)\big) \right\|_\infty. \quad (6)$$

An iterative process is used to determine which $\mathcal{G}_{zw}(s, \Omega_j)$ and $\mathcal{S}(s, \Omega_j)$ have to be included in the optimization to ensure stability for all Ω in the speed range of the test rig (see [9]).

3.3. Adapted parametrization process

To incorporate the excitation from the PMSM in the optimization, an additional external force $\boldsymbol{F}_{d,\text{PMSM}}$ is introduced as an input to the plant model $\mathcal{P}$ (see Fig. 6). $\boldsymbol{F}_{d,\text{PMSM}}$ is added to $\boldsymbol{F}_{\text{PMSM}}$. Furthermore, a weighting function $\mathcal{W}_{F_{d,\text{PMSM}}}$ is introduced for $\boldsymbol{F}_{d,\text{PMSM}}$ in the weighted plant model $\mathcal{P}_\mathcal{W}$ (see Fig. 7). A fourth-order bandpass filter in $\mathcal{W}_{F_{d,\text{PMSM}}}$ ensures that the main excitation frequency of $\boldsymbol{F}_{d,\text{PMSM}}$ is $\Delta\omega_{\text{PMSM}} = 135\,\text{Hz}$ below the rotational speed Ω_j. Furthermore, $\boldsymbol{F}_{d,\text{PMSM}}$ is zero for $\Omega_j \leq \Delta\omega_{\text{PMSM}}$. Hence, $\mathcal{W}_{F_{d,\text{PMSM}}}$ is chosen as

$$\mathcal{W}_{F_{d,\text{PMSM}}}(s, \Omega_j) = \begin{cases} \dfrac{(0.02\,\omega_{d,j}s)^4}{\big(s^2 + 0.02\,\omega_{d,j}s + \omega_{d,j}^2\big)^4}\widehat{F}_{d,\text{PMSM}}\,\mathfrak{J} & \text{for } \omega_{d,j} > 0, \\ \qquad\qquad 0 & \text{for } \omega_{d,j} \leq 0 \end{cases} \quad (7)$$

$$\text{with } \omega_{d,j} = \Omega_j - \Delta\omega_{\text{PMSM}}.$$

$\mathfrak{J}$ is a 4×4 identity matrix since the force acts on two nodes in the stator and rotor model in both radial directions. $\widehat{F}_{d,\text{PMSM}}$ is the maximum amplitude of $\boldsymbol{F}_{d,\text{PMSM}}$.
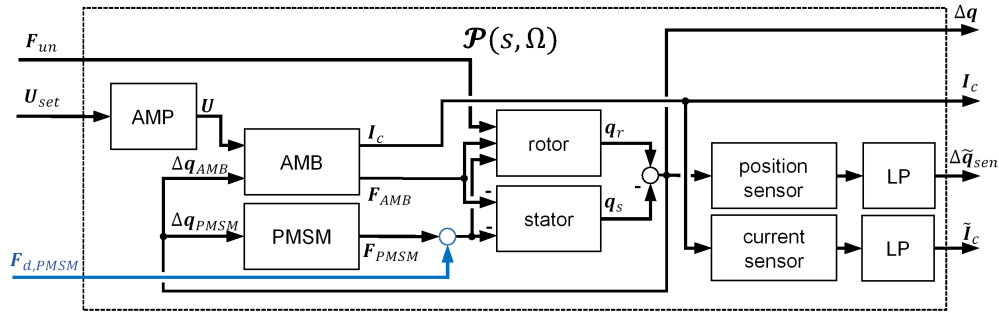
Fig. 6. Structure of the expanded plant model
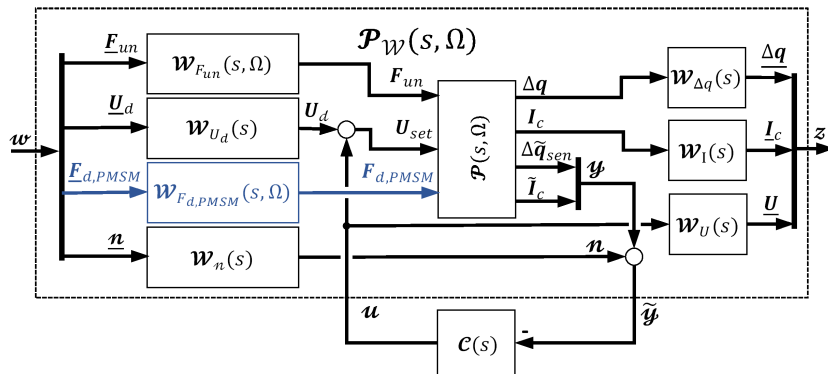
Fig. 7. Expanded, weighted model of the plant with the controller

4. Experimental investigation

The controller parameters were tuned with the adapted model, including the changed specimen geometry, and various $\widehat{F}_{d,\text{PMSM}}$. The goal was to tune the controller for the greatest possible $\widehat{F}_{d,\text{PMSM}}$ without the maximum output of the model becoming greater than one. The first tuned parameter set which was experimentally investigated, was tuned for an assumed force amplitude of $\widehat{F}_{d,\text{PMSM}} = 22\,\text{N}$, where the maximum output of the model started to approach one. Measured Campbell-diagrams of the rotor displacement with this new controller parameter set during run-ups with different acceleration rates are shown in Fig. 8.

The sidebands are not visible during a slow run-up with an acceleration rate of 150 rpm/s (see Fig. 8a, cf. Fig. 3a). With higher acceleration rates, the sidebands do occur, but with a lower

(a) 150 rpm/s

(b) 517.2 rpm/s

(c) 1 111.1 rpm/s

(d) 1 304.3 rpm/s
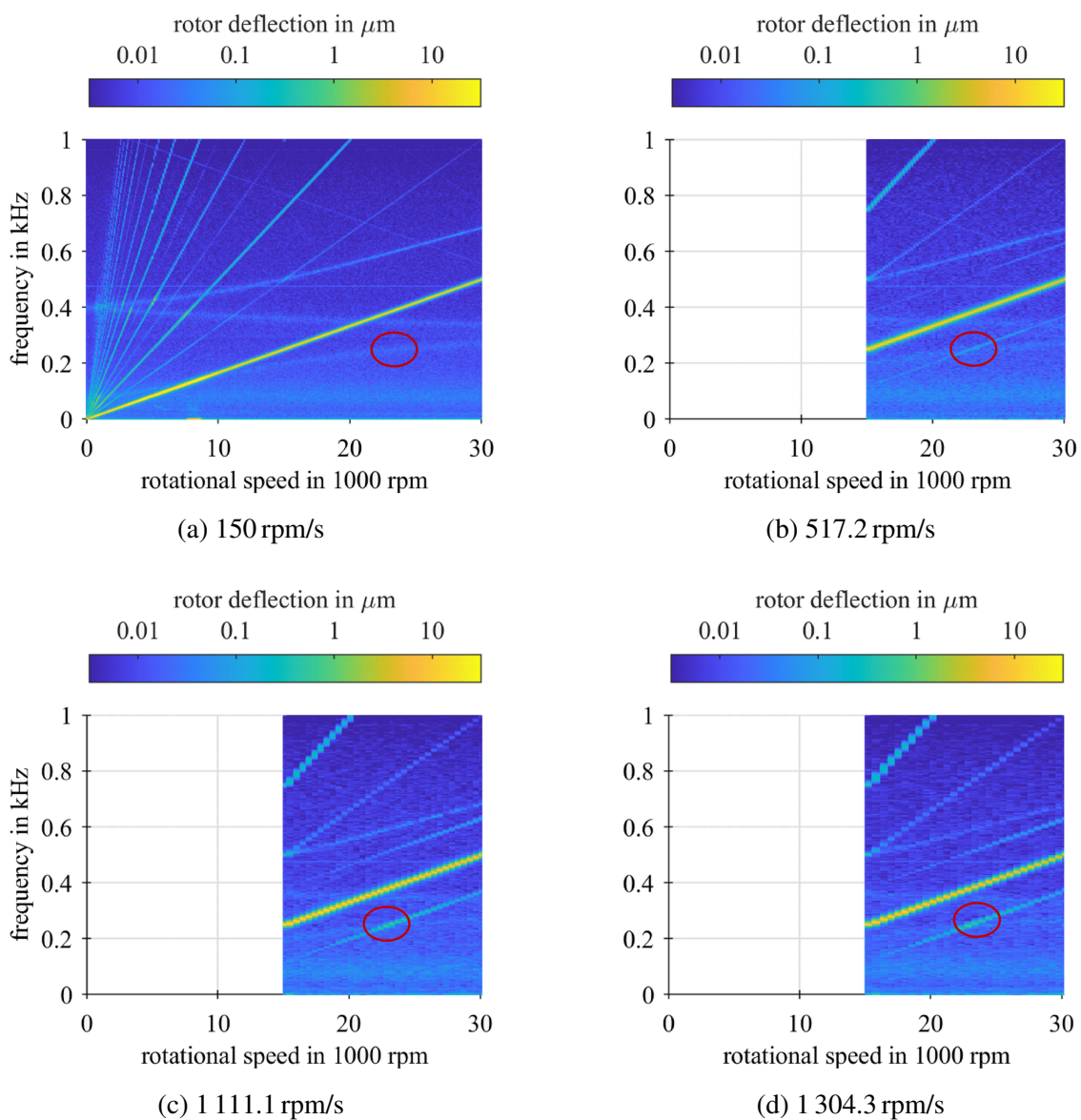
Fig. 8. Measured Campbell-diagram of the radial rotor displacement with the new controller parameter set during a run-up (a) from 0 rpm to 30 000 rpm in 200 s, (b) from 15 000 rpm to 30 000 rpm in 29 s, (c) from 15 000 rpm to 30 000 rpm in 13.5 s and (d) from 15 000 rpm to 30 000 rpm in 11.5 s. The red circle marks the subharmonic excitation of the third eigenmode

amplitude than with the old controller parameter set (cf. Table 2 in the Appendix). No accelerations faster than 330 rpm/s were possible during long-term operation with the old parameter set. However, more than 1 300 rpm/s were possible with the new parameter set with acceptable vibration levels. This increase in acceleration decreased the time per cycle by 68 s, which reduces the time it takes to perform 200 000 cycles by 155 days. The parameter optimization could be repeated with a higher $\widehat{F}_{d,\text{PMSM}}$, however, the achieved cycle time was acceptable.

5. Conclusion

Acceleration-dependent radial vibrations limited the performance of a test rig for fatigue tests of FRP cylinders after the specimen was replaced. These vibrations were significantly reduced by adjusting the utilized model and including an additional excitation in the parameter optimization of the radial AMB control. This allowed for faster cycles and reduced the total test duration. The second specimen was cycled for a total of 123 237 cycles until the test had to be stopped because of a fatigue crack in the aluminium hub.

In general, the described parameter tuning process for the AMB control can easily be adapted to different disturbances and changes in the system. It can also be applied to other systems with varying parameters, which can be described locally by linear transfer functions (cf. [2]). However, finding a constant controller which stabilizes a system for a wide range of situations might not always be possible because of limitations in the system, especially of the amplifier. Furthermore, the computation time for the optimization increases significantly with the order of the overall system. It also has to be noted that the result of the optimization might be a local minimum and it is advisable to repeat the optimization several times with different initial values.

Acknowledgements

References

[1] Ahrens, M., Kucera, L., Larsonneur, R., Performance of a magnetically suspended flywheel energy storage device, IEEE Transactions on Control Systems Technology 4 (5) (1996) 494–502. https://doi.org/10.1109/87.531916

[2] Apkarian, P., Gahinet, P., Buhr, C., Multi-model, multi-objective tuning of fixed-structure controllers, Proceedings of the 2014 European Control Conference (ECC), Strasbourg, 2014, pp. 856–861. https://doi.org/10.1109/ECC.2014.6862200

[3] Apkarian, P., Noll, D., Optimization-based control design techniques and tools, In: Encyclopedia of systems and control, J. Baillieul and T. Samad (editors), London, Springer, 2013, pp. 1–12. https://doi.org/10.1007/978-1-4471-5102-9_144-1

[4] Balas, G., Chiang, R., Packard, A., Safonov, M., Robust control toolbox 3: Getting started guide, Natick, The MathWorks, Inc., 2011.

[5] Barbaraci, G., Pesch, A. H., Sawicki, J. T., Experimental investigations of minimum power consumption optimal control for variable speed AMB rotor, Proceedings of the ASME International Mechanical Engineering Congress and Exposition, Vancouver, ASME – The American Society of Mechanical Engineers, 2010, pp. 1047–1056. https://doi.org/10.1115/IMECE2010-40044

[6] Beno, J. H., Thompson, R. C., Werst, M. D., Manifold, S. M., Zierer, J. J., End-of-life design for composite rotors, IEEE Transactions on Magnetics 37 (1) (2001) 284–289. https://doi.org/10.1109/20.911838

[7] Chiba, A., Fukao, T., Ichikawa, O., Oshima, M., Takemoto, M., Dorrell, D. G., Magnetic bearings and bearingless drives, Elsevier, 2005. https://doi.org/10.1016/B978-0-7506-5727-3.X5000-7

[8] Duan, G.-R., Howe, D., Robust magnetic bearing control via eigenstructure assignment dynamical compensation, IEEE Transactions on Control System Technology 11 (2) (2003) 204–215. https://doi.org/10.1109/TCST.2003.809253

[9] Franz, D., Jungblut, J., Rinderknecht, S., Controller parameterization and bias current reduction of active magnetic bearings for a flexible and gyroscopic spindle, Advanced Control for Applications 4 (3) (2022) 1–23. https://doi.org/10.1002/adc2.113

[10] Franz, D., Richter, M., Schneider, M., Rinderknecht, S., Homopolar active magnetic bearing design for outer rotor kinetic energy storages, Proceedings of IEEE International Conference on Electric Machines and Drives (IEMDC), San Diego, 2019, pp. 774–778. https://doi.org/10.1109/IEMDC.2019.8785389

[11] Franz, D., Schneider, M., Richter, M., Rinderknecht, S., Thermal behavior of a magnetically levitated spindle for fatigue testing of fiber reinforced plastic, Actuators 8 (2) (2019) 1–18. https://doi.org/10.3390/act8020037

[12] Gahinet, P., Apkarian, P., Decentralized and fixed-structure H_∞ control in MATLAB, Proceedings of the 50th IEEE Conference on Decision and Control and European Control Conference, Orlando, 2011, pp. 8205–8210. https://doi.org/10.1109/CDC.2011.6160298

[13] Hirata, M., Ohno, T., Nonam, K., Robust control of a magnetic bearing system using constantly scaled H_∞ control, Proceedings of the 6th International Symposium on Magnetic Bearings: ISMB6, Cambridge, 1998, pp. 713–722.
https://www.magneticbearings.org/publication/detail/ismb6_68/

[14] Hopf, T., Richter, M., Schüßler, B., Rinderknecht, S., Control strategies for highly gyroscopic outer rotors with diametral enlargement in active magnetic bearings, Actuators 11 (3) (2022) 1–19. https://doi.org/10.3390/act11030091

[15] Hutterer, M., Schrödl, M., Control of active magnetic bearings in turbomolecular pumps for rotors with low resonance frequencies of the blade wheel, Lubricants 5 (3) (2017) 1–15. https://doi.org/10.3390/lubricants5030026

[16] International Organization for Standardization, ISO 14839-3:2006 Mechanical vibration – Vibration of rotating machinery equipped with active magnetic bearings – Part 3: Evaluation of stability margin, 2006.

[17] Kuseyri, İ. S., Robust control and unbalance compensation of rotor/active magnetic bearing systems, Journal of Vibration and Control 18 (6) (2012) 817–832. https://doi.org/10.1177/1077546310397560

[18] Lanzon, A., Tsiotras, P., A combined application of $\mathcal{H}_\infty$ loop shaping and μ-synthesis to control high-speed flywheels, IEEE Transactions on Control Systems Technology 13 (5) (2005) 766–777. https://doi.org/10.1109/TCST.2005.847344

[19] Larsonneur, R., Design and control of active magnetic bearing systems for high speed rotation, Ph.D. thesis, ETH Zürich, 1990.

[20] Lösch, F., Identification and automated controller design for active magnetic bearing systems, Ph.D. thesis, ETH Zürich, 2002.

[21] Maslen, E. H., Sawicki, J. T., Mu-synthesis for magnetic bearings: Why use such a complicated tool?, Proceedings of ASME 2007 International Mechanical Engineering Congress and Exposition, Seattle, ASME – The American Society of Mechanical Engineers, 2008, pp. 1103–1112. https://doi.org/10.1115/IMECE2007-43910

[22] Maslen, E. H., Schweitzer, G., Magnetic bearings: Theory, design, and application to rotating machinery, Springer, Berlin, 2009. https://doi.org/10.1007/978-3-642-00497-1

[23] Mason, P., Nowe, D., Atallah, K., Soft magnetic composites in active magnetic bearings, Proceedings of IEE Colloquium on New Magnetic Materials – Bonded Iron, Lamination Steels, Sintered Iron and Permanent Magnets, London, 1998, pp. 1–4. https://doi.org/10.1049/ic:19980332

[24] Mushi, S. E., Lin, Z., Allaire, P. E., Design, construction, and modeling of a flexible rotor active magnetic bearing test rig, IEEE/ASME Transactions on Mechatronics 17 (6) (2012) 1170–1182. https://doi.org/10.1109/TMECH.2011.2160456

[25] Narita, M., Chen, G., Takami, I., Gain scheduling controller synthesis for active magnetic bearing based on parameter dependent LMI with convexity condition, Proceedings of the 2nd International Conference on Control and Robotics Engineering (ICCRE), Bangkok, 2017, pp. 63–67. https://doi.org/10.1109/ICCRE.2017.7935043

[26] Nonami, K., Ito, T., μ synthesis of flexible rotor-magnetic bearing systems, IEEE Transactions on Control System Technology 4 (5) (1996) 503–512. https://doi.org/10.1109/87.531917

[27] Noshadi, A., Shi, J., Lee, W. S., Shi, P., Kalam, A., Robust control of an active magnetic bearing system using H_∞ and disturbance observer-based control, Journal of Vibration and Control 23 (11) (2017) 1857–1870. https://doi.org/10.1177/1077546315602421

[28] Quurck, L., Richter, M., Schneider, M., Franz, D., Rinderknecht, S., Design and practical realization of an innovative flywheel concept for industrial applications, Technische Mechanik 37 (2–5) (2017) 151–160. https://doi.org/10.24352/UB.OVGU-2017-092

[29] Sawicki, J. T., Maslen, E. H., Bischof, K. R., Modeling and performance evaluation of machining spindle with active magnetic bearings, Journal of Mechanical Science and Technology 21 (6) (2007) 847–850. https://doi.org/10.1007/BF03027055

[30] Siva Srinivas, R., Tiwari, R., Kannababu, C., Application of active magnetic bearings in flexible rotordynamic systems – A state-of-the-art review, Mechanical Systems and Signal Processing 106 (2018) 537–572. https://doi.org/10.1016/j.ymssp.2018.01.010

[31] Steyn, S. J. M., van Vuuren, P. A., van Schoor, G., Multivariable H_∞ or centre of gravity PD control for an active magnetic bearing flywheel system, SAIEE Africa Research Journal 102 (3) (2011) 76–88. https://doi.org/10.23919/SAIEE.2011.8532174

[32] Schüßler, B., Hopf, T., Rinderknecht, S., Drop-downs of an outer rotor flywheel in different planetary touch-down bearing designs, Actuators 11 (2) (2022) 1–16. https://doi.org/10.3390/act11020030

[33] Tang, J., Zhao, S., Wang, Y., Wang, K., High-speed rotor's mechanical design and stable suspension based on inertia-ratio for gyroscopic effect suppression, International Journal of Control, Automation and Systems 16 (4) (2018) 1577–1591. https://doi.org/10.1007/s12555-017-0117-z

[34] Weitzel, T., Schneider, M., Franke, G., Glock, C. H., Rinderknecht, S., Sizing and operating a hybrid electric energy storage system using meta heuristics, Proceedings of the 8th International Conference & Workshop REMOO Energy, Venice, 2018.

[35] Zhou, K., Doyle, J. C., Essentials of robust control, Upper Saddle River, Prentice Hall, 1998.

Appendix

Table 1. Parameters of the PMSM with its inverter

Max. electric power	30 kW
Max. rotational speed	40 000 rpm
Max. phase current	70 A
Max. torque	9.6 Nm
Number of pole pairs	2
Number of slots in the stator	36
Switching frequency inverter	16 kHz

Table 2. Amplitude of the lower sideband and the 1st harmonic at the subharmonic resonance at 23 200 rpm

controller	acceleration	amplitude at 23 200 rpm	
		lower sideband	1st harmonic
old	150 rpm/s	0.04 μm	10.44 μm
old	300 rpm/s	0.28 μm	9.40 μm
old	750 rpm/s	1.48 μm	10.83 μm
old	1000 rpm/s	1.96 μm	10.21 μm
new	150 rpm/s	0.04 μm	10.51 μm
new	517 rpm/s	0.13 μm	8.46 μm
new	1 111 rpm/s	0.51 μm	8.05 μm
new	1 304 rpm/s	0.60 μm	6.28 μm
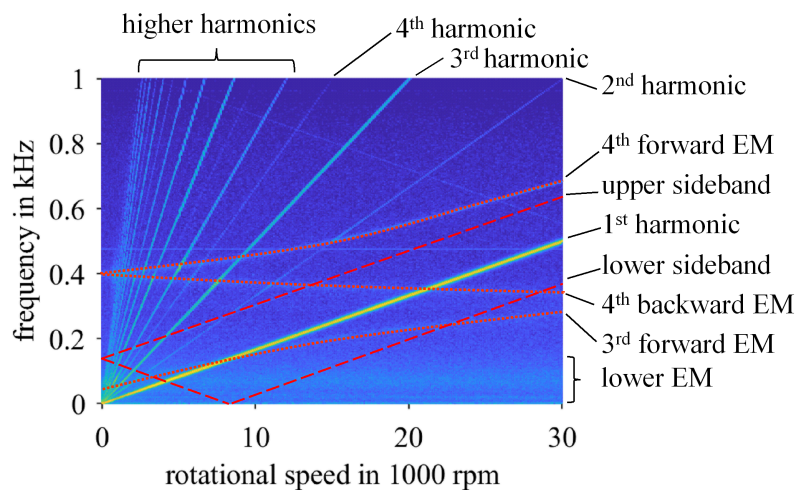
Fig. 9. Labelled Campbell-diagram of the radial rotor displacement during a run-up from 0 rpm to 30 000 rpm in 200 s (cf. Fig. 3a)